Title
Slowdown of Interhelical Motions Induces a Glass Transition in RNA

Journal
Biophysical Journal, 108(12)

ISSN
0006-3495

Authors
Frank, Aaron T
Zhang, Qi
Al-Hashimi, Hashim M
et al.

Publication Date
2015-06-01

DOI
10.1016/j.bpj.2015.04.041

Peer reviewed

Biophysical Journal Volume 108 June 2015 2876–2885

Article

Slowdown of Interhelical Motions Induces a Glass Transition in RNA

Aaron T. Frank,[1] Qi Zhang,[2] Hashim M. Al-Hashimi,[3] and Ioan Andricioaei[1,*]
[1]Department of Chemistry, University of California at Irvine, Irvine, California; [2]The University of North Carolina at Chapel Hill School of Medicine, Chapel Hill, North Carolina; and [3]Department of Biochemistry, Duke University School of Medicine, Durham, North Carolina

ABSTRACT RNA function depends crucially on the details of its dynamics. The simplest RNA dynamical unit is a two-way interhelical junction. Here, for such a unit—the transactivation response RNA element—we present evidence from molecular dynamics simulations, supported by nuclear magnetic resonance relaxation experiments, for a dynamical transition near 230 K. This glass transition arises from the freezing out of collective interhelical motional modes. The motions, resolved with site-specificity, are dynamically heterogeneous and exhibit non-Arrhenius relaxation. The microscopic origin of the glass transition is a low-dimensional, slow manifold consisting largely of the Euler angles describing interhelical reorientation. Principal component analysis over a range of temperatures covering the glass transition shows that the abrupt slowdown of motion finds its explanation in a localization transition that traps probability density into several disconnected conformational pools over the low-dimensional energy landscape. Upon temperature increase, the probability density pools then flood a larger basin, akin to a lakes-to-sea transition. Simulations on transactivation response RNA are also used to backcalculate inelastic neutron scattering data that match previous inelastic neutron scattering measurements on larger and more complex RNA structures and which, upon normalization, give temperature-dependent fluctuation profiles that overlap onto a glass transition curve that is quasi-universal over a range of systems and techniques.

INTRODUCTION

In orchestrating their wide repertoire of biochemical activities (1,2), RNA molecules involve a fine interplay among primary, secondary, and tertiary structures, and their dynamics, i.e., between folding and flexibility. For protein molecules, a variety of techniques including neutron scattering (3), x-ray diffraction (4), Mossbauer spectroscopy (5), light scattering (6), and molecular dynamics (MD) simulations (7–10) have provided evidence for a dynamical transition upon cooling. The protein glass transition involves a suddenly weaker temperature dependence of the average atomic fluctuations below a particular temperature T_g in the 200–240 K range. This is important because for proteins the abrupt increase in flexibility above T_g has been correlated with the onset of enzymatic function (11).

It is increasingly often being reported that RNA, too, can perform functions as complex as those of proteins, frequently with the involvement of larger conformational changes (12) that feature complete transformations in RNA secondary and tertiary structure needed for 1) catalysis or 2) recognition. It is therefore of interest to reveal the microscopic details behind the existence of a glass transition in RNA. In comparison to the numerous studies using a large battery of techniques for a wide variety of proteins (and, to some extent, for DNA (13–15)), less is known about the nature of dynamical transitions in RNA.

In recent experimental studies, inelastic neutron scattering (INS) was used to reveal a temperature-induced transition in hydrated tRNA (16,17) and yeast RNA (18) at a T_g in the vicinity of 220 K. These experimental results are significant because they suggest that the glass transition may also be a general feature of RNA systems and that, in similarity with proteins, the hydration water plays an important role. Specifically, the dehydrated tRNA samples did not undergo a dynamical transition, while the hydrated samples did, and the yeast RNA study showed that the transition temperature was the same as that for its hydration layer. Moreover, a recent all-atom simulation study analyzed water dynamics at various locations on the surface of two other RNA structures (the purine and preQ1 sensing riboswitch aptamers) as a function of temperature and showed that the dynamical transition exhibited by these RNA systems in similarity to the INS measurements of yeast- and t-RNA was accompanied by heterogeneous hydration dynamics (19).

However, the microscopic origins of the RNA glass transition (i.e., which specific sites and motional modes in the biomolecule show a change in their dynamics) remains yet to be identified, as they cannot be resolved in INS because signal is arising from an average over all hydrogen atoms throughout the entirety of the biomolecule.

Here, using MD simulations across the relevant temperature range, and backed by temperature-dependent nuclear

Submitted November 26, 2014, and accepted for publication April 21, 2015.
*Correspondence: andricio@uci.edu
Aaron T. Frank's present address is Department of Chemistry, University of Michigan, Ann Arbor, Michigan.
Editor: David Rueda.

0006-3495/15/06/2876/10 $2.00
http://dx.doi.org/10.1016/j.bpj.2015.04.041

magnetic resonance (NMR) relaxation experiments, we identify the microscopic origin of motional arrest. In the process, we take a look directly at the fundamental motions involved in the glass transition in RNA. We focus on the simplest dynamical entity upon which RNA motion hinges, the two-way junction, and in particular the transactivation response (TAR) RNA element (20), with basic and well-characterized structural dynamics (21,22). The TAR structure consists of two double-helical domains connected by a hinge and capped by a loop (see Fig. 1).

The advantage of using NMR relaxation observables over inelastic neutron scattering ones is that motion can be resolved at particular sites in the molecule, specifically here at several isotopically labeled ^{15}N-H bonds situated at different positions within the three-dimensional atomic structure of the molecule. Moreover, NMR can be used to distinguish between different motional modes such as localized bond librations versus collective motions of domains (23). NMR quantifies motion through the relaxation rate of nuclear spins in the N-H bonds, which, in its turn, depends on the orientational autocorrelation functions $C(t) = \langle P_2[\vec{\mu}(0)\cdot\vec{\mu}(t)]\rangle$ of the unit bond vector $\vec{\mu}(t)$, where $P_2(x) = (3x^2 - 1)/2$ is the second-order Legendre polynomial and brackets denote ensemble averaging. The most popular method for interpreting relaxation data (such as R_1, R_2, and nuclear Overhauser effect (NOE)) in terms of the bond motion is the Lipari-Szabo model free approach (24), in which the dynamics of bond vectors are described by amplitudes (order parameter, S^2) and corresponding time constants (τ) as obtained through the parameterization of $C(t)$. The extent of spatial restriction of a certain N-H bond vector is quantified by its order parameter S^2, which takes values in the interval [0,1]; higher S^2 values correspond to more restricted bond motion, and the limiting values $S^2 \rightarrow 0$ and $S^2 \rightarrow 1$ correspond to isotropic free rotation and frozen motion, respectively. Values of S^2 computed from MD simulations have been compared to those obtained from experiments (25–28); typical values for NH and CH bonds in proteins and nucleic acids are on the average at ~0.87 (29,30) at room temperature. For bond vectors undergoing complex internal motion, a two-exponential form (with a fast timescale, τ_f and a slow timescale, τ_s) is used (31),

$$C(t) = S^2 + \left(1 - S_f^2\right)e^{-t/\tau_f} + \left(S_f^2 - S^2\right)e^{-t/\tau_s}, \quad (1)$$

where the long-time, tail value of the time-correlation function is $S^2 = S^2_f S^2_s$, with the subscripts denoting fast (picosecond timescale, extreme narrowing limit) and slow (nanosecond timescale) motions, respectively. Expressions for R_1, R_2, and NOE, can be derived for this interpretation of the internal motions and fit to experimental data. Underlying Eq. 1 is the assumption that internal and overall motions are not correlated, and for the extended formalism that the fast and slow internal motions are also not correlated. Because the major contribution of large-amplitude, low-frequency slow motions to S^2_s is expected to come from the back-and-forth hinging of the two helical domains around the bulge (see Fig. 1), NMR bond vectors placed strategically through the structure in a proper reference frame (see below) can detect this relative motion. The fast component S^2_f would simply correspond to a background, extremely-rapid librational motion of the bond vector. Here, our combination of MD and NMR techniques shows that, at room temperature, TAR-RNA performs motions with the fast component in both domain I and domain II and the slow component consisting of the hinge bending of domain II relative to domain I (see Fig. 1 *c*). Upon decreasing temperature, the slow component slows down and vanishes at ~220 K, while the fast dynamics survives below this temperature.

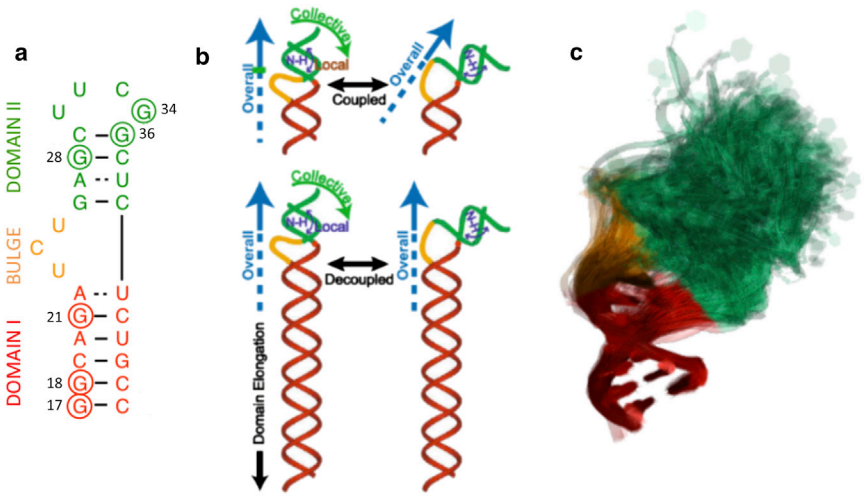

FIGURE 1 RNA motions detected by NMR and MD. (*a*) Secondary structure of HIV-1 TAR. Highlighted are domain I (*red*), bulge (*orange*), and domain II (*green*). Residues, G28, G34, and G36 in domain I, and G17, G18, and G21 in domain II, for which slow and, respectively, fast S^2 NMR data were measured, are circled. (*b*) Domain elongation. For TAR-RNA, collective interdomain motions (structures above) are coupled to overall tumbling; this makes NMR detection of internal motions difficult. Decoupling collective motions is performed by elongation of domain I (structures below); this effectively renders overall alignment parallel to the long axis of the RNA. (*c*) To mimic elongation in MD, we superpose MD snapshots relative to domain I only. Motions in domain I (*red*) represent fast internal motions (mostly bond librations). Motions in domain II (*green*) include fast motion and a slow component due to interhelical motions relative to domain I. To see this figure in color, go online.

MATERIALS AND METHODS

Temperature dependence of S^2 from MD simulations

We simulated the onset of restricted motion across T_g by computer calculations of TAR dynamics. We computed directly the temperature-dependent S^2 values by performing constant-temperature MD on TAR at each temperature in the range 150–300 K in 12.5-K increments. We used the GROMACS package (32) with nucleic acids force-field parameter set CHARMM36 (33). The starting structure was generated from sequence using the RNA structure prediction program FARNA (34); the modified RNA construct used in the NMR experiments precluded the use of the NMR structure that was solved for the wild-type construct (35). Briefly, a set of 1000 models was generated that was based on the sequence and the secondary structure of the HIV-1 TAR construct used in the NMR experiments (see Fig. 1). The lowest energy model was minimized to remove steric clashes, and was charge-neutralized using sodium counterions and solvated with TIP3P water (36) within a triclinic cell with an 8.5 Å buffer between the largest dimension of the RNA in each direction and the faces of the cell. Periodic boundary conditions were used and electrostatics were calculated with the particle-mesh Ewald method (37). RNA was first energy-minimized, then gradually heated to 300 K over the course of 0.4 ns. The 300-K system was then cooled in 12.5-K, 20-ps steps to 150 K. At the end of the process, 13 systems (at T = 150.0, 162.5, 175.0, 187.5, 200.0, 212.5, 225.0, 237.5, 250.0, 262.5, 275.0, 287.5, and 300.0 K) were generated. For each of these systems, constant temperature simulations were initiated from the saved coordinates and velocities. Trajectories were 10 ns long. These trajectories were used for the bond-vector relaxation analysis, as described below. Additional independent simulations were carried out: eight independent replicas were propagated for 80-ns total time at each of the temperatures of 150, 200, 250, and 300 K. The eight replicas had starting structures generated as described above, except that they were initialized with different random velocities, each drawn from the Maxwell distribution for the respective temperature. The eight replica, 80-ns composite trajectories each run at the four temperatures of 150, 200, 250, and 300 K were used in the principal component analysis described below. All constant-temperature MD simulations were carried out using a Nosé-Hoover thermostat (38,39), and the SHAKE (40) algorithm was used to constrain covalent bonds involving hydrogen, allowing the use of a 2-fs time-step. To mimic the elongation strategy in the NMR experiment, all trajectory snapshots were overlaid onto a common reference structure involving root-mean-square fitting of all heavy atoms of helical domain I only (i.e., the domain actually elongated in the experiment, the lower domain; see Fig. 1 *c* and Musselman et al. (30) for details). This strategy, on the one hand, reflected faithfully the reference frame inherent in the experiment and, on the other, effectively lifted the nonuniqueness in removing overall rotation of flexible molecules (41), given that domain I maintained a relatively rigid helical structure.

The values S^2 were calculated from the trajectories as the long-time limit of the orientational autocorrelation $\lim_{t\to\infty} C(t) = \langle P_2(\vec{\mu}(0)\cdot\vec{\mu}(\infty))\rangle = P_2[(\sum_i\sum_j\langle\mu_i\mu_j\rangle^2)^{1/2}]$ (42), with μ_i the ith Cartesian component of the bond vector $\vec{\mu}$ whose S^2 value is calculated, and the averaging is over all the snapshots of this vector oriented in the molecular reference frame aligned along the major axes of (the lower) domain I. For direct comparison, we first calculated S^2 for the G28, G34, and G36 N1-H1 bond vectors, i.e., exactly for those labeled in the samples of the NMR experiments (see below). The agreement between the computed and NMR derived $1 - S^2(T)$ is shown Fig. 2 *c*. While the computed S^2 value overestimates bond-vector motion (a general feature for RNA simulations of NMR motion (30)), the position of T_g (238 vs. 236 K for the MD and NMR, respectively) are quite similar. For comparison with INS studies, $\langle\Delta x^2\rangle$ was also computed along the trajectories. To mimic INS experimental observables, $\langle\Delta x^2\rangle$ values were computed using hydrogen atom positions only. Unlike with the S^2 calculations, the trajectories were not aligned relative to domain I, rather overall rotation was removed by aligning snapshot relative to all heavy atoms in an arbitrarily chosen reference structure. Excellent agreement is observed between $\langle\Delta x^2\rangle$ obtained from experimental INS on hydrated tRNA and those computed for TAR-RNA. Moreover, the temperature-dependent $\langle\Delta x^2\rangle(T)$ profiles mirrors closely the experimental and computed $1 - S^2(T)$ profiles (Fig. 2, *b* and *c*).

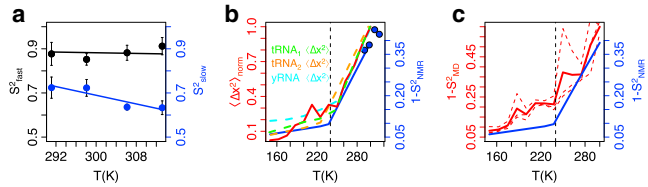

FIGURE 2 Temperature-dependent TAR dynamics. (*a*) Experimental S^2_s (*blue*) and S^2_f (*black*) values obtained from NMR relaxation measured at 291.11, 298.11, 306.18, and 313.17 K. Values are averaged over the isotopically labeled N-H bond vectors (see Fig. 1 *a*). (*b*) Comparison between measured $1-S^2(T)$ (obtained via S^2_f, S^2_s extrapolation, see text) (*blue*) and the computed mean-square fluctuations $\langle\Delta x^2\rangle(T)$ (*red*) of TAR-RNA. Included are the measured S^2_s (*blue dots*) scaled such that they coincide with the extrapolated NMR $1-S^2(T)$ profile. Also shown are INS-based $\langle\Delta x^2\rangle(T)$ values measured for tRNA (data from Caliskan et al. (16) and Chu et al. (17) in *green* and *orange*, respectively) and yeast RNA (from Chu et al. (18), in *cyan*). (*c*) Comparison between computed and NMR $1-S^2(T)$ profiles. Included are the computed profiles for G28, G34, and G36 N-H bond vectors (*red dashed lines*) and their average (*red solid line*). Vertical line at 240 K in (*b*) and (*c*) is a visual guide to T_g. To see this figure in color, go online.

Temperature dependence of S^2 from NMR

As an independent test of the results from MD on TAR dynamics, we also gauged the temperature dependence of the order parameters (S^2) by using ^{15}N imino nitrogen relaxation measurements for the N1-H1 bond vectors of residues G17, G18, and G21 from domain I and G28, G34, and G36 from domain II; the NMR-detected motion was measured over a range of decreasing temperatures. A problem that needed to be surmounted for the analysis of NMR relaxation for TAR was that its moment of inertia is small enough that its overall tumbling motion as a rigid body couples to the internal, slow dynamical relaxation (τ_s) embodied in Eq. 1. It was therefore crucial to find experimental means to decouple internal from overall motions for our RNA. For this, a domain-elongation technique was employed (23), in which NMR-invisible bases elongated the lower helical domain I (in *red* in Fig. 1), thereby anchoring overall tumbling by significantly slowing down rigid-body motion (see Fig. 1 *b*). Thus, while NH bonds from domain I provided a mean to characterize fast timescale motions, the NH bonds located in the upper helical domain, domain II (*green helix* in Fig. 1), could be used to probe both fast and slow motional modes. The imino ^{15}N longitudinal (R_1) and transversal ($R_2^{(CPMG)}$) relaxation rates and ^{1}H-^{15}N NOEs were measured closely following the procedure in Zhang et al. (23) at temperatures of 291.11, 298.11, 306.18, and 313.17 K, calibrated using standard methods employing an ethanol sample. The temperature dependence of the overall correlation time for extended-TAR derived from model free analysis of the NMR relaxation data exhibited the expected linear dependence with respect to temperature/viscosity, yielding a surface area of ~5.0 × 10^3 Å^2, which is consistent with calculations (~6.2 × 10^3 Å^2) based on the extended-TAR hydrodynamic shape (see Fig. S1 in the Supporting Material). This provided us with independent support for the overall validity of the model-free analysis and the measured ^{15}N relaxation data.

RESULTS

The relaxation data were analyzed using the extended model free formalism (Eq. 1), from which the motional descriptor $S^2(T)$ was determined for each labeled bond from either $S^2(T) = S^2_f(T)$ or $S^2(T) = S^2_f(T)S^2_s(T)$. To begin, complete profiles for the temperature dependence of the fast and slow order parameters, i.e., $S^2_{f,s}(T)$, were obtained by least-square linear fitting $S^2_f(T)$ and $S^2_s(T)$, over the range of available temperatures, each to $S^2_{f,s} = a_{f,s}T + b_{f,s}$, respectively, where $a_{f,s}$ and $b_{f,s}$ are the four linear fit parameters. Both $S^2_f(T)$ and $S^2_s(T)$ were then extrapolated to 1 (no motion); similar extrapolations for NMR data on proteins were shown to be valid by Lee and Wand (43). The slow (ns) component S^2_s had a stronger temperature dependence than the fast (ps) one (see Fig. 2 *a*). The amplitude of fast bond librations (S^2_f) exhibited much weaker variations within the examined temperature range than slow librations, in agreement with the previous NMR study of methyl-bearing side-chain motions (43), and were assumed to freeze out at ~0 K ($S^2_f = 1$). Our domain elongation approach, however, allowed us, for the first time (to our knowledge), to probe the temperature dependence of the amplitude of the slower collective helix motional mode (S^2_s). Unlike for S^2_f, a much steeper linear temperature dependence is observed for S^2_s over the temperature range measured. Remarkably, linear extrapolation of the best-fit line suggests that the collective helix motions freeze out near a temperature ($T = 236$ K) that is very similar to the protein glass transition temperature.

Altogether, the NMR extrapolations reflect the fact that, due to the arrested dynamics in the glassy state, $S^2_s(T) \rightarrow 1$ (slow motion becomes so slow that it is no longer detected in NMR relaxation, an aspect also valid for INS experiments, given their time-window sensitivity (44)) when $T \rightarrow T_g$, where T_g is the temperature at which slow motion halts. On the other hand, because of the extreme narrowing limit for fast motions, $S^2_f(T) \rightarrow 1$ only when T goes all the way to 0 K, i.e., when all local librations of the vectors become effectively frozen (in a classical mechanics sense).

Comparison with existing and backcalculated INS data

We have also analyzed, from the above extrapolation, the T-dependence of the value of $1 - S^2$ (where $S^2 = S^2_f S^2_s$), averaged over all NMR-measured bonds in domain II (which has both fast local and slow collective motions). This is because $1 - S^2$ is, roughly, the NMR motional equivalent of Cartesian atomic fluctuations $\langle(\Delta x)^2\rangle$ measurable in inelastic neutron scattering; they both gauge fluctuations, albeit through different means, i.e., via first-order versus second-order Legendre polynomials for the former and the latter, respectively (45). (An additional difference is that NMR can also measure individual bond motions before averaging over all the molecules, therefore enabling detection at virtually any molecular site). Remarkably, the temperature extrapolation for the average of $1 - S^2$ as described above for TAR strongly resembled the temperature dependence of the mean-square fluctuations $\langle(\Delta x)^2\rangle$ measured in the inelastic neutron scattering studies of tRNA (16,17) and yeast RNA (18). In these INS experiments, the typical signature of the glass transition (as seen in RNA, as well as in proteins and in DNA) is marked by a biphasic change at T_g in the slope of two roughly linear T-dependences as the mean-square fluctuations $\langle(\Delta x)^2\rangle$ in the atomic displacements. The glass transition is similarly evidenced here by $1 - S^2$ as a function of temperature. Taken collectively, our data suggest that collective helix motions are primarily those that are arrested at the glass transition. Fig. 2 *b* shows this T dependence of $1 - S^2$ for TAR-RNA, together with the mean-square deviation fluctuations for tRNA and yeast RNA from INS measurements with data from Caliskan et al. (16) and Chu et al. (17,18) and with our simulated TAR-RNA inelastic neutron scattering data, i.e., with the TAR-RNA mean-square deviation fluctuations of hydrogens from our MD simulations (see below). A remarkable similarity in the values of T_g and a universality in the overall shape of normalized fluctuation descriptors across various RNA systems and experimental methods was observed when scaling all INS and NMR and simulation data (see Fig. 2 *b*).

Principal component analysis and dynamics in Euler angle space

We further sought to reveal the contributions of the important degrees of freedom to the changes in the relevant RNA motions upon decreasing the temperature in the MD simulations. We used, for the T-dependent trajectories, a principal component analysis of a covariance matrix of coordinate fluctuations $\mathbf{A} = \{a_{ij}\} = \{\overline{(q_i - \overline{q_i})(q_j - \overline{q_j})}\}$, where q_i and q_j are mass-weighted atomic coordinates (46). The eigenvector matrix $\mathbf{V}$ of $\mathbf{A}$ can then be determined as the solution of the eigenvalue problem $\mathbf{AV} = \xi\mathbf{V}$, where ξ is a diagonal matrix with elements ξ_k, with ξ_k being the eigenvalue of the kth eigenvector. The eigenvectors are ranked according to their eigenvalues from low-frequency, large-amplitude motions, to high-frequency, small-amplitude motions. The conformations sampled along MD trajectories can be projected along a given mode to provide a time series, $y_k(t)$ being the involvement of that mode in the conformational change,

$$y_k(t) = \left(\mathbf{r}(t) - \mathbf{r}_{\text{ref}}\right) \cdot \mathbf{y}_k, \tag{2}$$

where the index k runs over the principal modes, $\mathbf{r}(t)$ is the $3N$-dimensional vector of atomic positions sampled along the trajectory, $\mathbf{r}_{\text{ref}}$ is the reference vector (here taken to be

the average structure along the trajectory), and $\mathbf{y}_k$ is the kth principal mode.

Projecting trajectories onto the first principal components (PCs) allowed us to visualize the conformational space explored along the modes, accounting for the largest variability in the data at each temperature (47,48). In Fig. 3 we plot the density of the projections of each snapshot in the composite trajectory along the first two PCs at 150, 200, 250, and 300 K, respectively. Below T_g, the space sampled consists of a set of disconnected clusters, or puddles, on an effective free energy surface, with motion arrested (each of the puddles are filled by the conformations the replicas visit). As temperature increases, the puddles coalesce. This is indicative of the onset of basin-to-basin dynamics, akin to a lakes-to-sea transition. This leads to a picture of the biphasic T dependence of the fluctuations in which, at temperatures above T_g, the conformational ensemble experiences motion in a broad effective free energy well, with soft curvature. At temperatures below T_g, we have a superposition of several small stiff wells, the motion between which takes places on such a long timescale that it evades detection (by the measurements or simulations) and only the contribution from fast bond-vector motion in each well is detected. Because fluctuations in effective harmonic wells, assuming equipartition, are inversely proportional to their stiffness (curvature), this explains the two slopes above and below T_g.

As discussed above, the analysis of the NMR relaxation data leads to the extrapolation $S^2_s(T) \rightarrow 1$ when $T \rightarrow T_g$. The lakes-to-sea picture above provides us with a qualitative description of this dynamical transition in terms of collective coordinates captured by the first few PCs spanning the slow manifold. However, it does not give direct insights into which molecular substructures activate their motion as temperature is increased beyond T_g. For further analysis, we also computed S^2 order parameters for bond vectors in all the residues throughout the structure of TAR, not just for those labeled in the NMR experiments. The data are presented in Fig. 4 *a*, where we compare the temperature dependence of $1-S^2(T)$ for bond vectors in domain I, domain II, and the bulge. This shows that bond-vector motion in domain II (and to some extent in the adjacent bulge) comprises the structures involved in the dynamical arrest. While the bond vectors residing in domain II exhibited the characteristic biphasic $1-S^2(T)$ profile, domain I bond vectors were devoid of this feature (see Fig. 4 *a*). Further insight emerged when the contributions of the first few PCs to $\langle \Delta x^2 \rangle(T)$ values were plotted as a function of temperature (see Fig. 4 *b*). As the rank of the PCs increased, the biphasic character of the $\langle \Delta x^2 \rangle(T)$ diminished. The lower-frequency PCs (e.g., PC1), which account for the slowest motional modes of TAR, exhibit the distinct biphasic T-dependence, in contrast to the higher frequency PCs (e.g., PC5 and higher), which account for faster motional modes. Because the strongest signature arises from the first three PCs, the slow manifold of interhelical junctions is roughly three-dimensional, and not merely a back-and-forth hinging of the upper helix relative to the lower one as the static structure would suggest. The dimensionality of three is needed to describe the full three interhelical orientation defined by the Euler angles α_h, β_h, and γ_h, which account for the twisting about domain I, bending between the two domains, and twist about domain II. To characterize the motions responsible for this transition we calculated, following the protocol in Bailor et al. (49) at each temperature, the ranges of α_h, β_h, and γ_h and then characterized, by three-dimensional angular binning, the volume of the three-dimensional Euler-angle space explored by the upper domain II. This allowed us to then gauge the fraction $\Omega(T) = \int_T d\alpha_h d\beta_h d\gamma_h / \int_{T_{\mathrm{ref}}} d\alpha_h d\beta_h d\gamma_h$ of the allowed

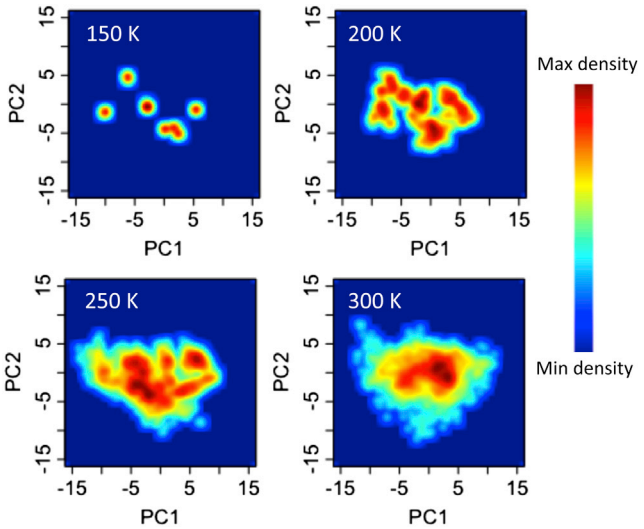

FIGURE 3 Visualizing the probability densities on TARs conformational space at different temperatures. Heat maps of the projection of the coordinates of trajectories simulated at 150, 200, 250, and 300 K onto the first and second PCs. As temperature is increased, the underlying conformational landscape is flooded akin to a lakes-to-sea transition on an effective free energy surface. To see this figure in color, go online.

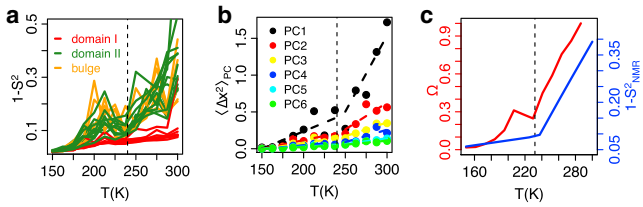

FIGURE 4 Dissecting the slow from the fast manifold through their respective temperature-dependent dynamics. (*a*) Computed $1\text{-}S^2(T)$ profiles of C'_1-H'_1 bond vectors residing in the lower domain I (*red*), upper domain II (*forest green*), and bulge (*orange*) of TAR. (*b*) Mean-square fluctuations $\langle \Delta x^2 \rangle(T)$ profiles calculated from the first six PCs. (*c*) Temperature-dependence of allowed topological space Ω (from MD simulations) gauged by the interhelical three-dimensional Euler-angle volume normalized relative to 300 K (see text). Extrapolated NMR $1-S^2(T)$ experimental profile (*blue line*) is included for comparison. To see this figure in color, go online.

topological space sampled by all TAR replicas simulated at a certain temperature T relative to the reference temperature T_{ref} = 300 K. Remarkably, we observe in Ω the same biphasic T-dependence that we observed in the previous results, and again, with an apparent dynamical transition 238 K (see Fig. 4 *c*). This result supports the view that the onset of the slow glass transition corresponds precisely to the arrest of the slow component of interhelical motions in TAR-RNA. (See also Movie S1 in the Supporting Material displaying the temperature dependence of the available volume in Euler angle space.)

Non-Arrhenius dependence of bond-vector relaxation

Glassy materials are often categorized as being strong or fragile glasses, depending on how their relaxation depends on temperature (50). Fragile glasses exhibit a markedly non-Arrhenius dependence as the glass transition is approached from above, and this feature has been linked to a heterogeneity in the underlying dynamics (51). Because we showed that distinct fast and slow regions coexist in TAR, making it consistent with the dynamical heterogeneity picture, we were interested in assessing its fragility. We therefore calculated the second-order Legendre polynomial orientational autocorrelation function P_2 for the C1′-H1′ bond vectors for all residues in domain II of TAR from the trajectories generated at T = 150.0, 162.5, 175.0, 187.5, 200.0, 212.5, 225.0, 237.5, 250.0, 262.5, 287.5, and 300.0 K (the 237.5 K trajectory was excluded from the calculation because it yielded a nonconverged outlier in the relaxation time). The maximum correlation time (τ_{max}) was set to 500 ps and the resulting correlation functions were fit to single exponentials. At each temperature, the characteristic time τ obtained from the fits was averaged over all the C1′-H1′ bond vectors in domain II to give $\langle\tau\rangle$. Fig. 5 shows the plot of $\log(\langle\tau\rangle)$ as a function of inverse temperature T_g/T, revealing a non-Arrhenius dependence. Points with $T_g/T < 1$ were too few to unequivocally assign fragile or strong behavior in the spirit of the Angell plot (50). However, we could assess the degree to which the plot of $\log(\langle\tau\rangle)$ over the entire range of T_g/T suggests a nonlinear model as a better fit for the data than a linear (Arrhenius) model. For this purpose we used the F-test (52) for the null hypothesis that the polynomial model does not provide a statistically significant better fit (the null hypothesis is rejected when the F-statistic is greater than critical F value (F-critical), which typically corresponds to the 0.05 false-rejection probability). The analysis confirmed that the F-statistic exceeded the F-critical, indicating non-Arrhenius dependence, further pointing to the heterogeneity (53) observed in the characteristics of individual bond-vector relaxation at different sites within the molecule.

Thus, collectively, the analyses of our simulations in terms of order parameters, mean-square fluctuations, principal components, the picture of the lakes-to-sea transition, relaxation and the available angular space, together with the INS-measured fluctuation data, bolster the assumption used to analyze the NMR relaxation data. It provides a general description of the motional details at the onset of an RNA glass transition, with similar values of T_g for the various analyses and the various systems.

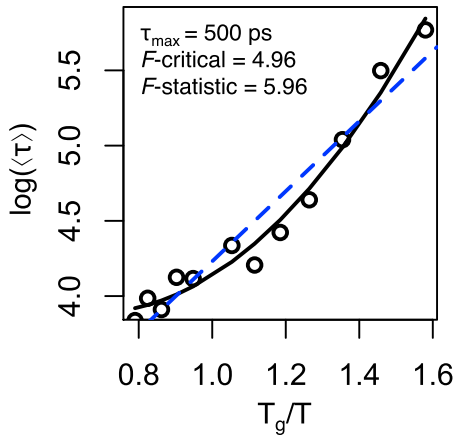

FIGURE 5 Relaxation time as a function of inverse temperature. At each temperature, $\langle\tau\rangle$ corresponds to the mean characteristic time obtained from exponential fits to the orientational P_2 autocorrelation function over bond vectors in domain II of TAR. The F-statistic compared the linear Arrhenius (*dashed blue*) and the second-order polynomial (*solid black*) fit to the data of the critical F value (F-critical). Because the F-statistic exceeds F-critical, the second-order polynomial provides a better fit than the linear model that is statistically significant. To see this figure in color, go online.

DISCUSSION

We used NMR relaxation experiments and MD simulations to investigate the temperature-dependent motions of the simplest dynamical motif in structured RNAs—a two-way junction, that of a TAR RNA element. Analysis of the relaxation properties measured for a set of isotopically labeled N-H bond vectors in terms of an model free formalism and using a particular domain-elongation technique that enabled the decomposition of slow and fast motion revealed that a slow component of the motion undergoes a dynamical transition near T_g = 236 K. This experimental value was corroborated by the MD simulations, which probed directly the T dependence of motion and yielded a value of T_g = 238 K. The $1-S^2(T)$ profiles obtained from the experiment and simulations exhibited remarkable correspondence with the $\langle\Delta x^2\rangle(T)$ profiles obtained from INS measurements on hydrated tRNA and yeast RNA, as well as to the corresponding $\langle\Delta x^2\rangle(T)$ profiles for TAR calculated from our computer simulations. There have been many efforts by INS to identify the main structural relaxation process(es) responsible for the glass transitions. While the inelastic neutron scattering atomic fluctuations profiles computed for TAR are shown to accurately reproduce experimental data on tRNA

and yeast RNA, INS data cannot give site-specific information of the motional arrest. Here, we reemphasize that NMR may be used to uncover 1) the complex motional modes of relaxation with temporal and spatial resolution and 2) that this can be done at the site-specific level. Our study revealed heterogeneity in the order parameters, which were different at different positions within the molecule (i.e., they were spatially heterogeneous), as well as having different characteristic relaxation timescales; the freezing of the slow dynamics of particular sites of the molecule was responsible for the dynamical transition. The presence of slow and fast regions, coexisting within the molecule, is inviting further investigations into the question of where RNA is positioned in the spread of relaxations between the strong and fragile extremes of glass-forming liquids (54).

The PC analysis revealed a slow-manifold dimensionality of ~3, in accord with an analysis of the three Euler angles needed to describe the relative orientation of domain II relative to domain I. It showed that it is not only the azimuth and the elevation of the upper helix II relative to domain I that comprise the slow manifold, but also that the twisting around the helical axis contributes, with a minor contribution from the bulge upon which the interhelical motions hinge. TAR is known to undergo complex interdomain motions, allowing it to sample various conformational substates. The ability to sample all interhelical orientations has significant implications for TAR's functionality in ligand binding (55,56). Moreover, the temperature-dependent changes in RNA junction angular orientations (roughly equivalent to Ramachandran plots for amino acids) may address the question of the role of conformational biases of simple helical junctions, which can in turn influence RNA folding stability and specificity (57), thereby offering a link to the connection between *T*-arrest and function (akin to those seen in proteins). For example, in a study of NMR relaxation on proteins, Lee and Wand (43) observed three distinct peaks in the distribution of methyl order parameters. This observation was taken as evidence for the existence of three classes of motion and was related to a hierarchical energy landscape model; it was also used to suggest an alternative origin for the protein glass transition. However, more detailed studies on a wider variety of proteins have showed more global, or continuum-type, changes throughout the solvated protein (9,58) rather than due to only a subset of side chains. Similar studies to those herein but on RNA with increasingly large tertiary structure and higher-complexity interhelical junctions (three-way, four-way, etc.) may reveal novel tiers of motions or a continuum such as that found for general glass transitions in proteins. What is also interesting is that both tRNA (a four-way junction) and yeast RNA have much more complicated shapes than TAR. Yet the dynamical arrest signature occurs at nearly the same *T*, and the RNA glass transition occurs with a nearly universal biphasic fluctuation profile across a range of observables (root-mean-square fluctuations, order parameters, topological Euler space).

Furthermore, we showed that interhelical junctions serve as hinges, the slowdown of which result in an abrupt change in RNA internal viscosity to an extent similar to that of proteins (59), and whose *T*-dependence would be the equivalent of viscosity increases in real glass formers (50). Because structure is not needed to measure Euler angles, interhelical dynamics could be probed in principle by residual dipolar couplings (22,60); further *T*-dependent NMR studies on a wider variety of RNAs may reveal the extent to which the glass transitions for various elements are fragile or strong (50).

MD simulations of nucleic acids are limited by the accuracy of the empirical force field used. Relative to proteins, RNA force-field stability is a particularly difficult balancing act, as it involves larger charge densities, a broader range of interaction types, and more motion (61,62). Unbalanced nucleic-acid force fields can result in unstable trajectories that fail to capture the structural and dynamical properties of RNA (63,64), with errors especially pronounced for small systems ($<$10 nt) and long simulation times (μs and beyond) (65). In order to mitigate issues associated with force-field errors, in this work we utilized the most recent CHARMM nucleic acid force field, CHARMM36 (33), which has been demonstrated to result in more stable trajectories when compared to the previous CHARMM27 force field. While a difference between the measured S^2 order parameters and those derived from MD simulations was observed, the MD values for all bonds were simply shifted downward relative to the experimental ones. This qualitative preservation of the S^2 profiles was previously seen for both proteins (28) and RNA (66), suggesting more dynamics in the simulation than probed within the observational time window of NMR. The temperature-dependent motional profiles derived from NMR and MD were also similar upon a constant shift, suggesting that the results probing the freeze-out of nanosecond dynamics in TAR are valid.

It is also of interest to discuss the role of the solvent in the context of our description of RNA dynamical arrest. The INS studies on tRNA and yeast RNA have shown that the glass transition disappears upon dehydration, but whether water enslaves the RNA, or the similarity of the water and the RNA transition is only a coincidence, are still open questions—in particular because there are indications that the transition temperature itself is hydration-dependent (67). In our sea-to-lakes picture, the role of the water is folded in the effective free energy surface that includes the water component. We expect that dehydrated RNAs have a different sea structure, the dynamics of which remain superpositions of harmonic motions. This view is consistent with a model that collectively accounts for all evidence to date simply by assuming that motions of biomolecules in solution slow down continuously with temperature (68). In this model, the observed dynamical transition may be

no more than the appearance of motions within the observational timescale window of the experimental apparatus used. Under this assumption, it can be that for dry conditions, biomolecules change their characteristic energy landscape in such a way that at temperatures above the T_g value for hydrated conditions, the motions are slower than those able to be experimentally detected. In the equilibrium picture, this can be understood as the survival of just a few inherent structures (69) upon dehydration, interconversion between these being slow.

As structural and dynamical experiments on increasingly larger RNA structures become available, we may unravel more details about the nature of molecular motions, their partitioning across different functional modes, their couplings, and their different responses to temperature changes. Another question that remains open concerns DNA, for which signatures of a glass transition have been found in both simulation (13,14) and experiment (15). For long DNA, low-frequency bending modes are important; for short DNA fragments, fraying will probably play a key role. More complex motions may also be revealed when four-way junctions, quadruplexes, knots, minicircles, or supercoils are studied for their complex dynamics at larger μm-scales (70). Further examination of temperature response for broader classes of nucleic acid structures, natural (71,72) or man-made (73), is likely to unfold new details involving dynamical arrest. Taken together, our results extend the importance of the dynamical transition in the biomolecular realm. The similar values of T_g revealed so far, and the common behavior at the dynamical crossover, may well be indicative of universal features of the underlying energy landscapes of an even wider range of biological systems.

SUPPORTING MATERIAL

Two figures and one movie are available at http://www.biophysj.org/biophysj/supplemental/S0006-3495(15)00491-9.

AUTHOR CONTRIBUTIONS

A.T.F., Q.Z., H.M.A.-A., and I.A. designed research; A.T.F. and Q.Z. performed research; H.M.A.-A. and I.A. analyzed data; and A.T.F., Q.Z., H.M.A.-A., and I.A. wrote the article.

ACKNOWLEDGMENTS

This work was generously supported in part by the National Science Foundation Career Award program (grant No. CHE-0918817, to I.A.) and by the National Institutes of Health (grant No. R01 AI066975, to H.M.A.).

REFERENCES

1. Lilley, D. M. 1999. Structure, folding and catalysis of the small nucleolytic ribozymes. *Curr. Opin. Struct. Biol.* 9:330–338.
2. Williamson, J. R. 2000. Induced fit in RNA-protein recognition. *Nat. Struct. Biol.* 7:834–837.
3. Doster, W. 1991. The glass transition anomalies of myoglobin in the light of mode coupling theory. *Mod. Phys. Lett. B.* 5:1407–1414.
4. Frauenfelder, H., G. A. Petsko, and D. Tsernoglou. 1979. Temperature-dependent x-ray diffraction as a probe of protein structural dynamics. *Nature.* 280:558–563.
5. Parak, F., E. N. Frolov, …, V. I. Goldanskii. 1981. Dynamics of met-myoglobin crystals investigated by nuclear gamma resonance absorption. *J. Mol. Biol.* 145:825–833.
6. Caliskan, G., A. Kisliuk, and A. P. Sokolov. 2002. Dynamic transition in lysozyme: role of a solvent. *J. Non-Cryst. Solids.* 868:307–310.
7. Vitkup, D., D. Ringe, …, M. Karplus. 2000. Solvent mobility and the protein 'glass' transition. *Nat. Struct. Biol.* 7:34–38.
8. Réat, V., R. Dunn, …, J. C. Smith. 2000. Solvent dependence of dynamic transitions in protein solutions. *Proc. Natl. Acad. Sci. USA.* 97:9961–9966.
9. Curtis, J. E., M. Tarek, and D. J. Tobias. 2004. Methyl group dynamics as a probe of the protein dynamical transition. *J. Am. Chem. Soc.* 126:15928–15929.
10. Meinhold, L., J. C. Smith, …, A. H. Zewail. 2007. Picosecond fluctuating protein energy landscape mapped by pressure temperature molecular dynamics simulation. *Proc. Natl. Acad. Sci. USA.* 104: 17261–17265.
11. Rasmussen, B. F., A. M. Stock, …, G. A. Petsko. 1992. Crystalline ribonuclease A loses function below the dynamical transition at 220 K. *Nature.* 357:423–424.
12. Al-Hashimi, H. M., and N. G. Walter. 2008. RNA dynamics: it is about time. *Curr. Opin. Struct. Biol.* 18:321–329.
13. Norberg, J., and L. Nilsson. 1996. Glass transition in DNA from molecular dynamics simulations. *Proc. Natl. Acad. Sci. USA.* 93:10173–10176.
14. Kumar, P., Z. Yan, …, H. E. Stanley. 2006. Glass transition in biomolecules and the liquid-liquid critical point of water. *Phys. Rev. Lett.* 97:177802.
15. Chen, S.-H., L. Liu, …, E. Mamontov. 2006. Experimental evidence of fragile-to-strong dynamic crossover in DNA hydration water. *J. Chem. Phys.* 125:171103.
16. Caliskan, G., R. M. Briber, …, A. P. Sokolov. 2006. Dynamic transition in tRNA is solvent induced. *J. Am. Chem. Soc.* 128:32–33.
17. Chu, X.-Q., E. Mamontov, …, Q. Zhang. 2013. Temperature dependence of logarithmic-like relaxational dynamics of hydrated tRNA. *J. Phys. Chem. Lett.* 4:936–942.
18. Chu, X.-Q., E. Fratini, …, S.-H. Chen. 2008. Observation of a dynamic crossover in RNA hydration water, which triggers a dynamic transition in the biopolymer. *Phys. Rev. E Stat. Nonlin. Soft Matter Phys.* 77:011908.
19. Yoon, J., J.-C. Lin, …, D. Thirumalai. 2014. Dynamical transition and heterogeneous hydration dynamics in RNA. *J. Phys. Chem. B.* 118: 7910–7919.
20. Rosen, C. A., J. G. Sodroski, and W. A. Haseltine. 1985. The location of *cis*-acting regulatory sequences in the human T cell lymphotropic virus type III (HTLV-III/LAV) long terminal repeat. *Cell.* 41:813–823.
21. Dethoff, E. A., A. L. Hansen, …, H. M. Al-Hashimi. 2008. Characterizing complex dynamics in the transactivation response element apical loop and motional correlations with the bulge by NMR, molecular dynamics, and mutagenesis. *Biophys. J.* 95:3906–3915.
22. Salmon, L., G. Bascom, …, H. M. Al-Hashimi. 2013. A general method for constructing atomic-resolution RNA ensembles using NMR residual dipolar couplings: the basis for interhelical motions revealed. *J. Am. Chem. Soc.* 135:5457–5466.
23. Zhang, Q., X. Sun, …, H. M. Al-Hashimi. 2006. Resolving the motional modes that code for RNA adaptation. *Science.* 311:653–656.

24. Lipari, G., A. Szabo, and R. M. Levy. 1982. Protein dynamics and NMR relaxation: comparison of simulations with experiment. *Nature.* 300:197–198.

25. Pang, Y., M. Buck, and E. R. P. Zuiderweg. 2002. Backbone dynamics of the ribonuclease binase active site area using multinuclear (^{15}N and ^{13}CO) NMR relaxation and computational molecular dynamics. *Biochemistry.* 41:2655–2666.

26. Hornak, V., R. Abel, …, C. Simmerling. 2006. Comparison of multiple AMBER force fields and development of improved protein backbone parameters. *Proteins.* 65:712–725.

27. Trbovic, N., B. Kim, …, A. Palmer, III. 2008. Structural analysis of protein dynamics by MD simulations and NMR spin relaxation. *Proteins.* 71:684–694.

28. Maragakis, P., K. Lindorff-Larsen, …, D. E. Shaw. 2008. Microsecond molecular dynamics simulation shows effect of slow loop dynamics on backbone amide order parameters of proteins. *J. Phys. Chem. B.* 112:6155–6158.

29. Case, D. A. 2002. Molecular dynamics and NMR spin relaxation in proteins. *Acc. Chem. Res.* 35:325–331.

30. Musselman, C., Q. Zhang, …, I. Andricioaei. 2010. Referencing strategy for the direct comparison of nuclear magnetic resonance and molecular dynamics motional parameters in RNA. *J. Phys. Chem. B.* 114:929–939.

31. Clore, G. M., A. Szabo, …, A. M. Gronenborn. 1990. Deviations from the simple two-parameter model free approach to the interpretation of 15N nuclear magnetic relaxation of proteins. *J. Am. Chem. Soc.* 112:4989–4991.

32. Hess, B., C. Kutzner, …, E. Lindahl. 2008. GROMACS4: algorithms for highly efficient, load-balanced, and scalable molecular simulation. *J. Chem. Theory Comput.* 4:435–445.

33. Denning, E. J., U. D. Priyakumar, …, A. D. MacKerell, Jr. 2011. Impact of 2′-hydroxyl sampling on the conformational properties of RNA: update of the CHARMM all-atom additive force field for RNA. *J. Comput. Chem.* 32:1929–1943.

34. Das, R., and D. Baker. 2007. Automated de novo prediction of native-like RNA tertiary structures. *Proc. Natl. Acad. Sci. USA.* 104:14664–14669.

35. Aboul-ela, F., J. Karn, and G. Varani. 1996. Structure of HIV-1 TAR RNA in the absence of ligands reveals a novel conformation of the trinucleotide bulge. *Nucleic Acids Res.* 24:3974–3981.

36. Jorgensen, W. L., J. Chandrasekhar, …, M. L. Klein. 1983. Comparison of simple potential functions for simulating liquid water. *J. Chem. Phys.* 79:926–935.

37. Essmann, U., L. Perera, …, L. G. Pedersen. 1995. A smooth particle mesh Ewald method. *J. Chem. Phys.* 103:8577–8593.

38. Nosé, S. 1984. A unified formulation of the constant temperature molecular dynamics methods. *J. Chem. Phys.* 81:511–519.

39. Hoover, W. G. 1985. Canonical dynamics: equilibrium phase-space distributions. *Phys. Rev. A.* 31:1695–1697.

40. Ryckaert, J., G. Ciccotti, and H. Berendsen. 1977. Numerical integration of the Cartesian equations of motion of a system with constraints: molecular dynamics of *n*-alkanes. *J. Comput. Phys.* 23:327–341.

41. Zhou, Y., M. Cook, and M. Karplus. 2000. Protein motions at zero-total angular momentum: the importance of long-range correlations. *Biophys. J.* 79:2902–2908.

42. Henry, E. R., and A. Szabo. 1985. Influence of vibrational motion on solid-state lineshapes and NMR relaxation. *J. Chem. Phys.* 82:4753–4761.

43. Lee, A. L., and A. J. Wand. 2001. Microscopic origins of entropy, heat capacity and the glass transition in proteins. *Nature.* 411:501–504.

44. Becker, T., J. A. Hayward, …, J. C. Smith. 2004. Neutron frequency windows and the protein dynamical transition. *Biophys. J.* 87:1436–1444.

45. Bruschweiler, R., and P. Wright. 1994. NMR order parameters of biomolecules: a new analytical representation and application to the Gaussian axial fluctuation model. *J. Am. Chem. Soc.* 116:8426–8427.

46. Andricioaei, I., and M. Karplus. 2001. On the calculation of entropy from covariance matrices of the atomic fluctuations. *J. Chem. Phys.* 115:6289–6292.

47. Tournier, A. L., and J. C. Smith. 2003. Principal components of the protein dynamical transition. *Phys. Rev. Lett.* 91:208106.

48. Hong, L., D. C. Glass, …, J. C. Smith. 2013. Elastic and conformational softness of a globular protein. *Phys. Rev. Lett.* 110:028104.

49. Bailor, M. H., A. M. Mustoe, …, H. M. Al-Hashimi. 2011. 3D maps of RNA interhelical junctions. *Nat. Protoc.* 6:1536–1545.

50. Angell, C. A. 1995. Formation of glasses from liquids and biopolymers. *Science.* 267:1924–1935.

51. Debenedetti, P. G., and F. H. Stillinger. 2001. Supercooled liquids and the glass transition. *Nature.* 410:259–267.

52. Press, W., S. Teukolsky, …, B. P. Flannery. 2007. Numerical Recipes, 3rd Ed. The Art of Scientific Computing. Cambridge University Press, Cambridge, UK.

53. Frauenfelder, H., S. G. Sligar, and P. G. Wolynes. 1991. The energy landscapes and motions of proteins. *Science.* 254:1598–1603.

54. Angell, C. A., K. L. Ngai, …, S. W. Martin. 2000. Relaxation in glass-forming liquids and amorphous solids. *J. Appl. Phys.* 88:3113–3157.

55. Frank, A. T., A. C. Stelzer, …, I. Andricioaei. 2009. Constructing RNA dynamical ensembles by combining MD and motionally decoupled NMR RDCs: new insights into RNA dynamics and adaptive ligand recognition. *Nucleic Acids Res.* 37:3670–3679.

56. Stelzer, A., J. Kratz, …, H. Al-Hashimi. 2010. RNA dynamics by design: biasing ensembles towards the ligand-bound state. *Angew. Chem. Int.* 49:5731–5733.

57. Chu, V. B., J. Lipfert, …, D. Herschlag. 2009. Do conformational biases of simple helical junctions influence RNA folding stability and specificity? *RNA.* 15:2195–2205.

58. Best, R. B., J. Clarke, and M. Karplus. 2005. What contributions to protein side-chain dynamics are probed by NMR experiments? A molecular dynamics simulation analysis. *J. Mol. Biol.* 349:185–203.

59. Soranno, A., B. Buchli, …, B. Schuler. 2012. Quantifying internal friction in unfolded and intrinsically disordered proteins with single-molecule spectroscopy. *Proc. Natl. Acad. Sci. USA.* 109:17800–17806.

60. Stelzer, A. C., A. T. Frank, …, H. M. Al-Hashimi. 2009. Constructing atomic-resolution RNA structural ensembles using MD and motionally decoupled NMR RDCs. *Methods.* 49:167–173.

61. Banas, P., D. Hollas, …, M. Otyepka. 2010. Performance of molecular mechanics force fields for RNA simulations. Stability of UUCG and GNRA hairpins. *J. Chem. Theory Comput.* 6:3836–3849.

62. Zhu, X., P. E. M. Lopes, and A. D. MacKerell, Jr. 2012. Recent developments and applications of the CHARMM force fields. *Wires Comput. Mol. Sci.* 2:167–185.

63. Faustino, I., A. Pérez, and M. Orozco. 2010. Toward a consensus view of duplex RNA flexibility. *Biophys. J.* 99:1876–1885.

64. Banáš, P., P. Sklenovský, …, M. Otyepka. 2012. Molecular mechanism of preQ1 riboswitch action: a molecular dynamics study. *J. Phys. Chem. B.* 116:12721–12734.

65. Deng, N.-J., and P. Cieplak. 2010. Free energy profile of RNA hairpins: a molecular dynamics simulation study. *Biophys. J.* 98:627–636.

66. Musiani, F., G. Rossetti, …, P. Carloni. 2014. Molecular dynamics simulations identify time scale of conformational changes responsible for conformational selection in molecular recognition of HIV-1 transactivation responsive RNA. *J. Am. Chem. Soc.* 136:15631–15637.

67. Roh, J. H., R. M. Briber, …, A. P. Sokolov. 2009. Dynamics of tRNA at different levels of hydration. *Biophys. J.* 96:2755–2762.

68. Daniel, R. M., J. L. Finney, and J. C. Smith. 2003. The dynamic transition in proteins may have a simple explanation. *Faraday Discuss.* 122:163–190.

69. Stillinger, F. H., and T. A. Weber. 1984. Packing structures and transitions in liquids and solids. *Science.* 225:983–989.

70. Lillian, T. D., M. Taranova, …, N. C. Perkins. 2011. A multiscale dynamic model of DNA supercoil relaxation by topoisomerase IB. *Biophys. J.* 100:2016–2023.

71. Schmeing, T. M., and V. Ramakrishnan. 2009. What recent ribosome structures have revealed about the mechanism of translation. *Nature*. 461:1234–1242.

72. Wereszczynski, J., and I. Andricioaei. 2010. Free energy calculations reveal rotating-ratchet mechanism for DNA supercoil relaxation by topoisomerase IB and its inhibition. *Biophys. J.* 99: 869–878.

73. Mao, C., W. Sun, …, N. C. Seeman. 1999. A nanomechanical device based on the B-Z transition of DNA. *Nature*. 397:144–146.